

# Symmetry-breaking-induced nonlinear optics at a microcavity surface

Xueyue Zhang<sup>1,2,7,8</sup>, Qi-Tao Cao<sup>1,3,8</sup>, Zhuo Wang<sup>4</sup>, Yu-xi Liu<sup>2,5</sup>, Cheng-Wei Qiu<sup>4</sup>, Lan Yang<sup>6</sup>, Qihuang Gong<sup>1,3</sup> and Yun-Feng Xiao<sup>1,3\*</sup>

**Second-order nonlinear optical processes lie at the heart of many applications in both classical and quantum regimes<sup>1–3</sup>. Inversion symmetry, however, rules out the second-order nonlinear electric-dipole response<sup>1,4,5</sup> in materials widely adopted in integrated photonics (for example, SiO<sub>2</sub>, Si and Si<sub>3</sub>N<sub>4</sub>). Here, we report nonlinear optics induced by symmetry breaking<sup>6–10</sup> at the surface of an ultrahigh-Q silica microcavity under a sub-milliwatt continuous-wave pump. By dynamically coordinating the double-resonance phase matching, a second harmonic is achieved with an unprecedented conversion efficiency of 0.049% W<sup>-1</sup>, 14 orders of magnitude higher than that of the non-enhancement case<sup>11</sup>. In addition, the nonlinear effect from the intrinsic symmetry breaking at the surface<sup>8,12</sup> can be identified unambiguously, with guided control of the pump polarization and the recognition of the second-harmonic mode distribution. This work not only extends the emission frequency range of silica photonic devices, but also lays the groundwork for applications in ultra-sensitive surface analysis.**

The second-order nonlinearity in centrosymmetric materials originates from both the asymmetric potential experienced by the surface/interface layer and the bulk multipole response<sup>7,8</sup>. Different from breaking the bulk inversion symmetry, such as by exerting external strain<sup>13,14</sup> or an electric field<sup>15</sup>, second-harmonic generation (SHG) and sum-frequency generation (SFG) induced by the intrinsic symmetry breaking at a surface have been developed as non-invasive, label-free probes, for example, to measure the arrangement, adsorption or reaction of molecules on a surface<sup>12,16,17</sup>. However, such nonlinear optical signals at a surface are extremely weak even under a high-intensity pulsed pump. Typically, only thousands of second-harmonic photons are generated by a 50-fs pulse with 500 GW cm<sup>-2</sup> averaged intensity<sup>11</sup>, corresponding to a conversion efficiency of 1.7 × 10<sup>-16</sup>% W<sup>-1</sup>. Additionally, the bulk multipole effects disturb the deterministic study of surface properties, which has long been highly challenging<sup>8,11</sup>.

Nonlinear optical effects enhanced by microcavities have been extensively investigated since the 1980s<sup>18–25</sup>. For example, second-order nonlinearity had been studied in optical cavities made of materials without inversion symmetry<sup>24</sup>. Recently, second-order nonlinear signals were also observed in cavities with centrosymmetric materials<sup>26–30</sup>. These studies, however, required high pump power due to the lack of an efficient phase-matching method.

Moreover, the contributions of the nonlinear signal have not been identified deterministically yet, which has hindered potential applications. Here, we observe second-harmonic (SH) signals, originating from the symmetry-breaking-induced nonlinearity at a surface and the electric multipole response in the bulk (Fig. 1a), in a silica whispering-gallery microcavity<sup>31,32</sup> under a continuous-wave pump below 1 mW. The high conversion efficiency of 0.049% W<sup>-1</sup> results from doubly resonant enhancement of ultrahigh-Q modes (also known as perfect phase match), which is achieved by the thermal effect<sup>33</sup> and optical Kerr effect<sup>34</sup>. Importantly, we distinguish the surface symmetry-breaking-induced nonlinearity from the pure bulk nonlinear response by analysing the polarization of the pump mode and the electric-field distribution of the SH mode.

In the experiment, a silica microsphere (diameter ~62 μm) is pumped through a tapered optical fibre (waist diameter ~1 μm) at the 1,550 nm band (Fig. 1b). To collect the SH signal, a second fibre taper (waist diameter ~0.5 μm) designed for the 780 nm band is incorporated into the system (see Methods). The intrinsic quality factor for the pump cavity mode is 4.8 × 10<sup>7</sup>. Figure 1c shows a typical SH and the corresponding pump spectra measured by an electron-multiplying charge-coupled device (EMCCD) and an optical spectrum analyser, respectively. The SH signal appears at 777.75 nm when pumped at 1,555.14 nm, which deviates only 0.023% from the expected wavelength. Moreover, SH signals could be generated at different wavelengths when cavity modes are pumped from 1,545 nm to 1,565 nm (Fig. 1d). To compare the collected efficiencies of the two fibres, we optimize the fibre-cavity coupling so that the SH signal from the pump fibre is also observable. The maximum signal power from the pump fibre is still over one order of magnitude weaker than that from the signal fibre (Fig. 1e), resulting from the phase-mismatched light-collecting process of the pump fibre<sup>25</sup>. From either fibre, the SH signal is absent when the pump is off-resonance with the cavity mode, which helps to eliminate the possibility of spurious signals such as the second-order diffraction of the spectrometer grating.

Perfect phase matching is pivotal in achieving an efficient SHG, but the material and geometric dispersions obstruct the doubly resonant enhancement for both the pump and signal light<sup>22</sup>. The SH power can be derived from the coupled mode equations (see Supplementary Information):

<sup>1</sup>State Key Laboratory for Mesoscopic Physics and Collaborative Innovation Center of Quantum Matter, School of Physics, Peking University, Beijing, People's Republic of China. <sup>2</sup>Department of microelectronics and nanoelectronics, Tsinghua University, Beijing, People's Republic of China.

<sup>3</sup>Collaborative Innovation Center of Extreme Optics, Shanxi University, Shanxi, People's Republic of China. <sup>4</sup>Department of Electrical and Computer Engineering, National University of Singapore, Singapore, Singapore. <sup>5</sup>Institute of Microelectronics, Tsinghua University, Beijing, People's Republic of China. <sup>6</sup>Department of Electrical and Systems Engineering, Washington University in St. Louis, St. Louis, MO, USA. <sup>7</sup>Present address: Thomas J. Watson, Sr., Laboratory of Applied Physics, California Institute of Technology, Pasadena, CA, USA. <sup>8</sup>These authors contributed equally: Xueyue Zhang, Qi-Tao Cao. \*e-mail: yfxiao@pku.edu.cn

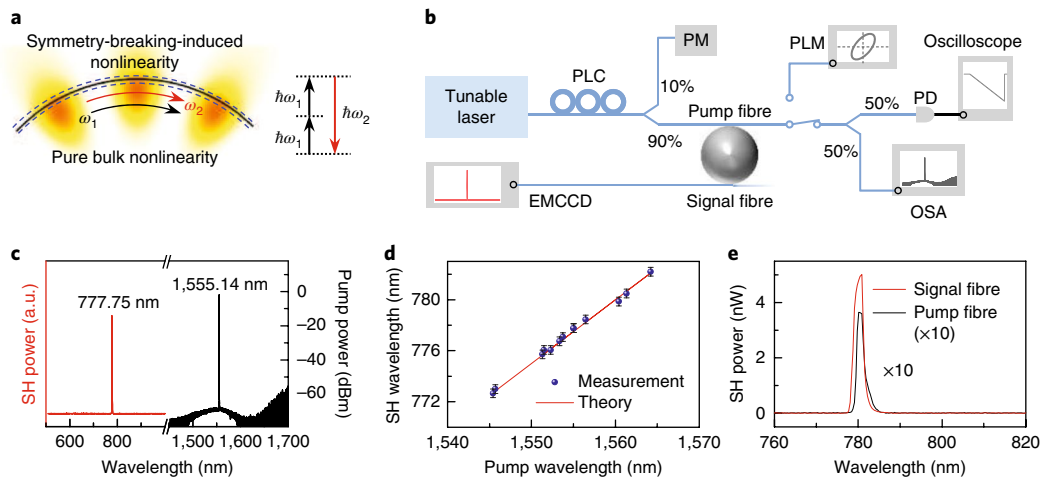


**Fig. 1 | Observation of cavity-enhanced SH signals.** **a**, SH signals are generated from the symmetry-breaking-induced nonlinearity at the cavity surface and the electric multipole response in the bulk. **b**, Experimental set-up. PM, power meter; PLM, polarimeter; OSA, optical spectrum analyser; PLC, polarization controller; PD, photodetector; EMCCD, electron-multiplying charge-coupled device spectrometer. **c**, Measured SH spectrum (red) and the corresponding pump (black). **d**, SH wavelengths versus the corresponding pump wavelengths for different modes. The blue dots with error bars showing the resolution of the EMCCD represent the experimental results (rigorous linear dependence with a slope of 0.5, red line). **e**, Comparison of the SH power collected by the pump fibre (10 times magnified) and the signal fibre.

$$P_2 = \frac{|g|^2}{\omega_2 \omega_1^2} \frac{4Q_2^2 / Q_{2e}}{4Q_2^2 (\omega_p / \omega_2 - 1)^2 + 1} \frac{16Q_1^4 / Q_{1e}^2}{[4Q_1^2 (\omega_p / \omega_1 - 1)^2 + 1]^2} P_1^2 \quad (1)$$

where the subscripts  $j=1, 2$  represent the pump and SH cavity modes with resonance frequencies  $\omega_j$ , respectively,  $Q_j$  is the loaded quality factor,  $Q_{je}$  is the external (coupling related) quality factor,  $g$  is the second-order nonlinear coupling strength between the two modes, and  $\omega_p$  and  $P_1$  are the pump frequency and power, respectively. Equation (1) shows that ultrahigh  $Q$  is indispensable in boosting the SH power, while the corresponding ultra-narrow linewidth also presents the challenge of achieving the double resonance. To compensate for the dispersion, we leverage the cavity-enhanced thermal<sup>33</sup> and optical Kerr effects<sup>34</sup> to dynamically manipulate the frequencies of both the pump and SH cavity modes.

The mechanism of the dynamic phase-matching process is illustrated in Fig. 2a. When the pump is on resonance with the cold cavity mode ( $\omega_{10}$ ), the SH signal is unlikely to be precisely on resonance with the SH mode ( $\omega_{20}$ ) because of the dispersion (top panel of Fig. 2a). Considering the thermal and Kerr effects of the pump light, both the pump and SH modes experience redshifts, and the wavelength of pump light should increase to catch the resonant mode, forming the non-Lorentzian shape in pump transmission (black curve in Fig. 2b). In the process of tuning pump light towards the pump resonant mode (states I–III in Fig. 2a,b), the SH signal can catch the SH mode ( $\omega_2$ ) at a certain pump wavelength, because the SH signal moves faster than the SH mode (Supplementary Information). The phase-matching condition is fulfilled at this time, and thus the SH power reaches a peak value (state II). By further increasing the pump wavelength, the SH signal passes the SH resonant mode, and its power diminishes rapidly (state III in Fig. 2a,b). The phase-matching process within the full tuning range is dynamically shown in Supplementary Video 1. In the experiment we tune the pump frequency in the range of the grey area in Fig. 2b with a given input power, and consequently obtain the SH power (blue dots in Fig. 2c), which agrees with the theoretical prediction.

Furthermore, the dependence of SH power on pump power is shown in Fig. 2d. Experimentally, under each input power, we search for the strongest SH output by tuning the pump wavelength. Varying the input power, a critical value occurs, at which

the pump and the SH are exactly on resonance with the respective cavity modes. In this case, the efficient SHG with the pump power of  $879 \mu\text{W}$  exhibits an unprecedented conversion efficiency  $P_2 / P_1^2$  of  $0.049 \text{ W}^{-1}$ , which is enhanced by over 14 orders of magnitude compared with the non-enhancement case<sup>11</sup>. Such an enhancement is the result of successful phase-matching described above and the ultrahigh quality factor of the cavity. Below the critical input power, the SH is off resonance within the full tuning range, resulting in the extremely weak SH power. Above the critical power, the SH power remains stable, because the intracavity power is almost steady when the signal is on resonance with the SH mode (Supplementary Information).

The SH signals originate from both the symmetry-breaking-induced nonlinearity at the surface and the electric multipole response in the bulk, described by the nonlinear coupling strengths  $g_{\text{SB}}$  and  $g_{\text{B}}$ , respectively. The former relies on the existence of the surface and can be directly influenced by surface properties, whereas the latter only depends on the electric-field distribution in the bulk. The former requires at least one of the pump or SH electric field to be perpendicular to the surface for utilizing the symmetry breaking at the surface, whereas the latter requires the SH electric field to be in the same direction with the pump (Supplementary Information). In a microsphere cavity with a diameter greater than dozens of micrometres, the electric field of a transverse electric (TE) mode is mainly along the polar direction, whereas a transverse magnetic (TM) mode has two main electric-field components along the radial and azimuthal directions. In both cases, the major electric-field components are about two orders of magnitude larger than the minor components. Therefore, under a TE-polarized pump, the SH from  $g_{\text{SB}}$  is TM polarized while the SH from  $g_{\text{B}}$  is TE polarized. Furthermore, TM and TE modes of a whispering gallery microcavity are not degenerate so that the symmetry-breaking-induced nonlinearity can be distinguished from the bulk contribution by measuring the polarization of the SH. Besides, theoretical analysis in the Supplementary Information also shows that the SH signal induced by  $g_{\text{SB}}$  exhibits an even polar distribution of the mode field (Fig. 3a), while the SH from  $g_{\text{B}}$  holds an odd polar distribution. In the experiment, we pump TE-polarized modes with the wavelength ranging from 1,541 nm to 1,560 nm, and the excited SH power is shown in Fig. 3b. Here the polarization of a pump mode

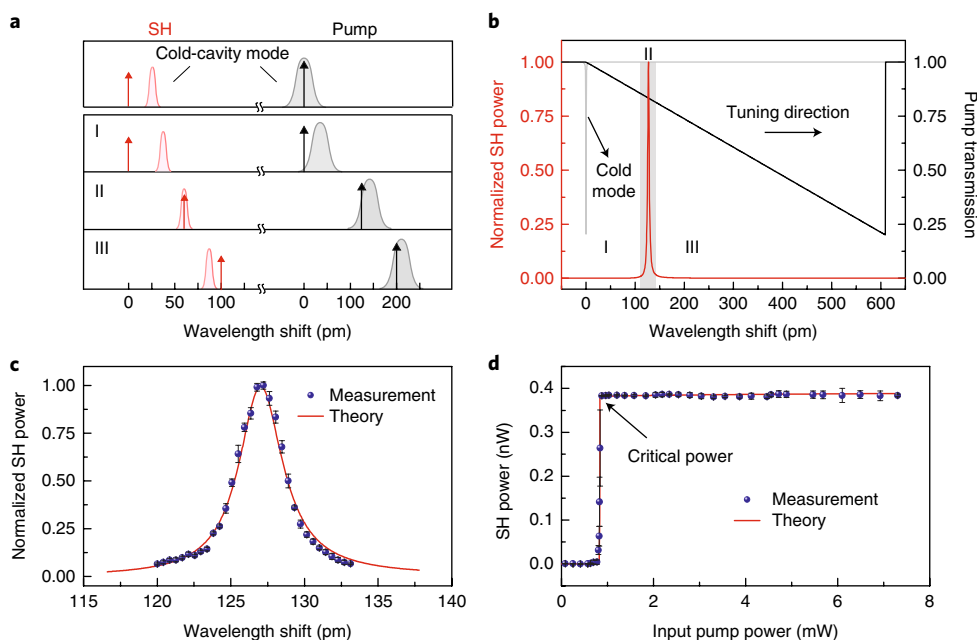


**Fig. 2 | Phase matching assisted by thermal and optical Kerr effects.** **a**, Schematic of the dynamic phase-matching process. The black (red) arrows represent the pump light (its SH) wavelength. The grey (red) Lorentzian shapes represent the pump (SH) cavity modes. States I–III show three typical cases with increasing pump wavelength but the same input power. **b**, Theoretical SH power (red curve) and pump transmission (black curve) at different pump wavelength shift relative to the cold-cavity mode (grey curve). I–III correspond to the three states in **a**. **c**, SH power versus pump wavelength shift with the input power of 4.46 mW. The wavelength range is the same as that of the grey area in **b**. **d**, Dependence of maximum SH power on the input power for the same pump mode. The fitting parameters are given in the Methods. The error bars in **c** and **d** represent the standard deviation of six repeated measurements.

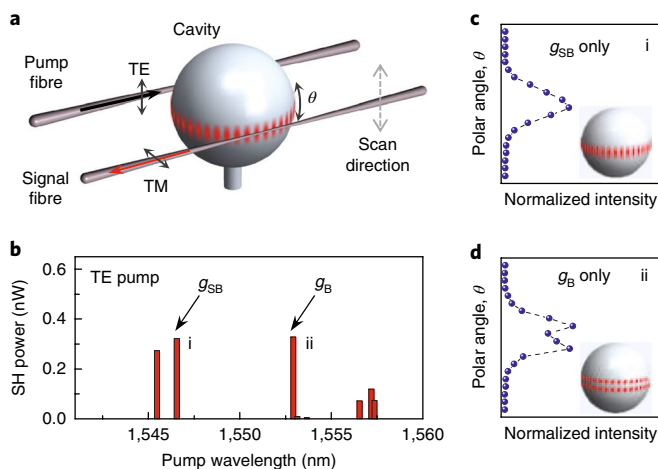


**Fig. 3 | Identification of symmetry-breaking-induced nonlinearity from the pure bulk response.** **a**, Schematic of the approach to obtain the symmetry-breaking-induced SH signal: pumping a TE mode and measuring the field distribution of the SH mode in the polar direction ( $\theta$ ). **b**, SH power measured with TE pump polarization, in the pump wavelength range from 1,541 nm to 1,560 nm. **c,d**, Measured even (**c**) and odd (**d**) polar-field distributions of the corresponding SH modes in **b**.

is confirmed by a polarimeter, and the polar-field distribution of a SH mode is obtained by measuring the dependence of SH intensity on polar angles (Fig. 3a and Supplementary Information). A symmetry-breaking-induced SH is achieved deterministically at pump wavelength of 1,546.71 nm, exhibiting only one maximum in the polar direction (Fig. 3c). The pure bulk SH (Fig. 3d), with two

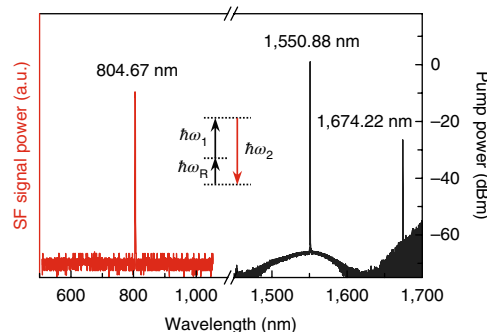


**Fig. 4 | Measured spectra of second-order sum-frequency generation.** The pump light ( $\omega_p$ ) and Raman light ( $\omega_r$ ) are summed to generate the sum-frequency (SF) signal ( $\omega_s$ ) with an input power of 7.33 mW.

maxima in the polar direction, is also observed under the pump of 1,553.07 nm.

With the second-order nonlinearity demonstrated above, SFG also arises, assisted by a Stokes Raman signal. Shown in Fig. 4 is a sum-frequency signal (804.67 nm), with the corresponding pump (1,550.88 nm) and the stimulated Raman scattering (1,674.22 nm). The deviation of the sum-frequency wavelength from the expected value (804.63 nm) is within the resolution of the spectrometers. The presence of the Raman signal and the perfect match with the SFG wavelength relation confirm that the source of the signal is the sum-frequency signal instead of the hyper-Raman scattering<sup>35</sup> that exhibits different selection rules and does not rely on the Raman signal.

The microcavity-enhanced optical nonlinearity resulting from symmetry breaking at a surface provides a new platform for

surface science and applications, for example, detection of molecules under submilliwatt pump power. In addition, the dynamic phase-matching method does not rely on the specific geometry and material of the cavity, making it a universal tool for surface nonlinear optics in various microcavity systems such as on-chip microtoroids, microdisks and microrings with different centrosymmetric materials such as Si and  $\text{Si}_3\text{N}_4$ . This work also shows potential for studying CMOS-compatible quantum optics mediated by the second-order nonlinearity.

### Online content

Any methods, additional references, Nature Research reporting summaries, source data, statements of data availability and associated accession codes are available at <https://doi.org/10.1038/s41566-018-0297-y>.

Received: 31 January 2018; Accepted: 12 October 2018;

Published online: 19 November 2018

### References

- Boyd, R. W. *Nonlinear Optics* (Elsevier, New York, 2003).
- Pereira, S., Xiao, M., Kimble, H. & Hall, J. Generation of squeezed light by intracavity frequency doubling. *Phys. Rev. A* **38**, 4931–4934 (1988).
- Kwiat, P. G. et al. New high-intensity source of polarization-entangled photon pairs. *Phys. Rev. Lett.* **75**, 4337–4341 (1995).
- Leuthold, J., Koos, C. & Freude, W. Nonlinear silicon photonics. *Nat. Photon.* **4**, 535–544 (2010).
- Moss, D. J., Morandotti, R., Gaeta, A. L. & Lipson, M. New CMOS-compatible platforms based on silicon nitride and Hydex for nonlinear optics. *Nat. Photon.* **7**, 597–607 (2013).
- Bloembergen, N., Chang, R. K., Jha, S. & Lee, C. Optical second-harmonic generation in reflection from media with inversion symmetry. *Phys. Rev.* **174**, 813–822 (1968).
- Shen, Y. R. Surface properties probed by second-harmonic and sum-frequency generation. *Nature* **337**, 519–525 (1989).
- Shen, Y. R. in *Fundamentals of Sum-Frequency Spectroscopy* Ch. 3 (Cambridge University Press, Cambridge, UK, 2016).
- Cazzanelli, M. & Schilling, J. Second order optical nonlinearity in silicon by symmetry breaking. *Appl. Phys. Rev.* **3**, 011104 (2016).
- Billat, A. et al. Large second harmonic generation enhancement in  $\text{Si}_3\text{N}_4$  waveguides by all-optically induced quasi-phase-matching. *Nat. Commun.* **8**, 1016 (2017).
- Tian, C. & Shen, Y. R. Recent progress on sum-frequency spectroscopy. *Surf. Sci. Rep.* **69**, 105–131 (2014).
- Sun, S., Tian, C. & Shen, Y. R. Surface sum-frequency vibrational spectroscopy of nonpolar media. *Proc. Natl Acad. Sci. USA* **112**, 5883–5887 (2015).
- Jacobsen, R. S. et al. Strained silicon as a new electro-optic material. *Nature* **441**, 199–202 (2006).
- Cazzanelli, M. et al. Second-harmonic generation in silicon waveguides strained by silicon nitride. *Nat. Mater.* **11**, 148–154 (2012).
- Timurdogan, E., Poulton, C. V., Byrd, M. & Watts, M. Electric field-induced second-order nonlinear optical effects in silicon waveguides. *Nat. Photon.* **11**, 200–206 (2017).
- Heinz, T. F., Tom, H. W. K. & Shen, Y. R. Determination of molecular orientation of monolayer adsorbates by optical second-harmonic generation. *Phys. Rev. A* **28**, 1883–1885 (1983).
- Corn, R. M. & Higgins, D. A. Optical second harmonic generation as a probe of surface chemistry. *Chem. Rev.* **94**, 107–125 (1994).
- Qian, S.-X., Snow, J. B., Tzeng, H.-M. & Chang, R. K. Lasing droplets: high-lighting the liquid-air interface by laser emission. *Science* **231**, 486–488 (1986).
- Braginsky, V., Gorodetsky, M. & Ilchenko, V. Quality-factor and nonlinear properties of optical whispering gallery modes. *Phys. Lett. A* **137**, 393–397 (1989).
- Lin, H.-B. & Campillo, A. CW nonlinear optics in droplet microcavities displaying enhanced gain. *Phys. Rev. Lett.* **73**, 2440–2443 (1994).
- Carmon, T. & Vahala, K. J. Visible continuous emission from a silica microphotonic device by third-harmonic generation. *Nat. Phys.* **3**, 430–435 (2007).
- Fürst, J. et al. Naturally phase-matched second-harmonic generation in a whispering-gallery-mode resonator. *Phys. Rev. Lett.* **104**, 153901 (2010).
- Del'Haye, P. et al. Optical frequency comb generation from a monolithic microresonator. *Nature* **450**, 1214–1217 (2007).
- Breunig, I. Three wave mixing in whispering gallery resonators. *Laser Photon. Rev.* **10**, 569–587 (2016).
- Jiang, X. et al. Chaos-assisted broadband momentum transformation in optical microresonators. *Science* **358**, 344–347 (2017).
- Gouveia, M. A. et al. Second harmonic generation and enhancement in microfibers and loop resonators. *Appl. Phys. Lett.* **102**, 201120 (2013).
- Lettieri, S. et al. Second-harmonic generation in hydrogenated amorphous- $\text{Si}_x\text{N}_y$  doubly resonant microcavities with periodic dielectric mirrors. *Appl. Phys. Lett.* **87**, 191110 (2005).
- Levy, J. S., Foster, M. A., Gaeta, A. L. & Lipson, M. Harmonic generation in silicon nitride ring resonators. *Opt. Express* **19**, 11415–11421 (2011).
- Asano, M. et al. Visible light emission from a silica microbottle resonator by second- and third-harmonic generation. *Opt. Lett.* **41**, 5793–5796 (2016).
- Xue, X. et al. Second-harmonic-assisted four-wave mixing in chip-based microresonator frequency comb generation. *Light Sci. Appl.* **6**, e16253 (2017).
- Vahala, K. J. Optical microcavities. *Nature* **424**, 839–846 (2003).
- Ward, J. & Benson, O. WGM microresonators: sensing, lasing and fundamental optics with microspheres. *Laser Photon. Rev.* **5**, 553–570 (2011).
- Carmon, T., Yang, L. & Vahala, K. J. Dynamical thermal behavior and thermal self-stability of microcavities. *Opt. Express* **12**, 4742–4750 (2004).
- Kippenberg, T. J., Spillane, S. M. & Vahala, K. J. Kerr nonlinearity optical parametric oscillation in an ultrahigh-Q toroid microcavity. *Phys. Rev. Lett.* **93**, 083904 (2004).
- Andrews, D. L. & Allcock, P. *Optical Harmonics in Molecular Systems: Quantum Electrodynamical Theory* (Wiley Online Library, Weinheim, 2002).

### Acknowledgements

The authors thank K. J. Vahala, M. Lončar, C. Tian, Y. R. Shen, T. F. Heinz, X. Yi, D. Lippolis, H. Wang, Q.-F. Yang and L. Shao for helpful discussions. This project is supported by the National Natural Science Foundation of China (grant nos. 11825402, 11654003, 61435001, 11474011, 61611540346 and 11527901), the National Key R&D Program of China (grant no. 2016YFA0301302), and the High-performance Computing Platform of Peking University.

### Author contributions

X.Z. and Q.-T.C. fabricated the microcavity samples, built the experimental set-up and carried out measurements. X.Z., Q.-T.C., Z.W., Y.-x.L. and C.-W.Q. built the theoretical model and performed numerical simulations. Y.-F.X., X.Z., Q.-T.C., C.-W.Q. and L.Y. wrote the manuscript with input from all co-authors. All the authors analysed the data and contributed to the discussion. Y.-F.X. conceived the idea and designed the experiment. Y.-F.X. and Q.G. supervised the project.

### Competing interests

The authors declare no competing interests.

### Additional information

**Supplementary information** is available for this paper at <https://doi.org/10.1038/s41566-018-0297-y>.

**Reprints and permissions information** is available at [www.nature.com/reprints](http://www.nature.com/reprints).

**Correspondence and requests for materials** should be addressed to Y.-F.X.

**Publisher's note:** Springer Nature remains neutral with regard to jurisdictional claims in published maps and institutional affiliations.

© The Author(s), under exclusive licence to Springer Nature Limited 2018

## Methods

**Cavity fabrication and the dual-fibre coupling system.** The silica microsphere was fabricated directly by a standard single-mode telecom fibre. We attenuated the fibre with a CO<sub>2</sub> laser, and obtained the microsphere by melting the end of the fibre. The dual fibres were fabricated respectively with standard single-mode fibre in the 1,550 nm and 780 nm bands, using different fabrication parameters. The influence of the signal fibre to  $Q$  is minor in the experiment. For example, the intrinsic  $Q$  of the pump mode in Fig. 1c before and after the incorporation of the signal fibre is  $4.8 \times 10^7$  and  $3.6 \times 10^7$ . The coupling between the signal fibre and the microsphere is adjusted while monitoring the transmission from the signal fibre with a tunable laser in the 780-nm band. The EMCCD and the pump laser are placed at the same side of the microsphere considering the linear momentum conservation requirement in SHG.

**Theoretical model and fitting.** The SHG can be described by the following coupled mode equations:

$$\frac{d\alpha_1}{dt} = \left[ i(\omega_p - \omega_1) - \frac{\kappa_{10} + \kappa_{1e}}{2} \right] \alpha_1 + \sqrt{\kappa_{1e}} s + ig^* \alpha_1^* \alpha_2 \quad (2)$$

$$\frac{d\alpha_2}{dt} = \left[ i(2\omega_p - \omega_2) - \frac{\kappa_{20} + \kappa_{2e}}{2} \right] \alpha_2 + ig\alpha_1^2 \quad (3)$$

where  $\alpha_j$  denotes the field amplitude in the cavity,  $s$  is the amplitude of the pump,  $\kappa_{je}$  denotes the external coupling rate and  $\kappa_{j0}$  ( $j=1, 2$ ) represents the intrinsic decay rate, which is related to the intrinsic  $Q$  as  $\kappa_{j0} = \omega_j/Q_{j0}$ ,  $g^*$  and  $a_1^*$  are the complex conjugates of the corresponding quantities and  $t$  is the time. To introduce the influence of the thermal and Kerr effects,  $\omega_1 = \omega_{10} - B_{11}|\alpha_1|^2$  and  $\omega_2 = \omega_{20} - B_{12}|\alpha_1|^2$  are used to describe the redshift of the cavity modes.  $B_{11}$  and  $B_{12}$  are determined by the effective thermal-induced refractive index change  $(\partial n/\partial T)_{\text{eff}}$  and the Kerr susceptibility  $\chi_{\text{Kerr}}$  (Supplementary Information). The steady-state solution of equations (2) and (3) with the shifted  $\omega_j$  are used to fit the measured data in Fig. 2c,d. The experimental data used in the fitting are cold-cavity pump frequency  $\omega_{10}/2\pi = 192.7901$  THz,  $\kappa_{10}/2\pi = 5.32$  MHz, cold-cavity resonance transmission  $T = 0.2$ .  $B_{11}$  is extracted to be  $4.93 \times 10^{21}$  rad s<sup>-1</sup> J<sup>-1</sup> from the pump wavelength shift at the peak in Fig. 2c and the corresponding intracavity energy. Figure 2c,d are both fitted with the same set of parameters, including the critical power of 832  $\mu$ W with the corresponding SH power of 0.381 nW. The loaded  $Q$  factor of the SH mode is fitted to be  $8.03 \times 10^6$ , the cold-cavity resonance frequency  $\omega_{20}/2\pi = 385.5784$  THz and the resonance shift coefficient  $9.29 \times 10^{21}$  rad s<sup>-1</sup> J<sup>-1</sup>. The fitted coefficient gives  $2B_{11}/B_{12} = 1.06$ .

## Data availability

The data that support the plots within this paper and other findings of this study are available from the corresponding author upon reasonable request.